Journal of Materials Chemistry C

ROYAL SOCIETY OF CHEMISTRY

PAPER

Cite this: J. Mater. Chem. C, 2021, 9, 14269

Laser-controlled projection of quantum dot dipoles using metal-oxide plasmonic metastructures: maintaining spin polarization memory†

Seyed M. Sadeghi, *[a] Waylin Wing,[b] Rithvik R. Gutha, ‡[a] Christina Sharp,[c] Dustin Roberts[a] and Chuanbin Mao [d]

Received 1st June 2021, Accepted 2nd September 2021

DOI: 10.1039/d1tc02532e

rsc.li/materials-c

It is known that the spontaneous emission of semiconductor quantum dots is mostly unpolarized when they are excited off-resonantly. The complete loss of polarization memory is associated with the ultrafast carrier scattering, leading to complete spin polarization relaxation. We study the application of metal-oxide plasmonic double-junction structures to transfer the excitation polarization memory of quantum dots to their spontaneous emission. These structures consist of arrays of metallic nanoantennas in the presence of heterostructures consisting of Au/Si Schottky junctions and Si/Al-oxide charge barriers. Our results show that by using such double-junction structures, one can control the states of polarization and intensity of the emission of quantum dots using the state of polarization of an off-resonant laser field. For achieving this, we explore the optical control of exciton–plasmon coupling using optical lattice modes caused by the arrays of metallic nanoantennas, and the application of the electrostatic field generated by the hot electrons captured at the Au/Si Schottky junction.

I Introduction

Controlling the state of polarization of spontaneous emission of semiconductor quantum dots (QDs) is an appealing subject of research with many unique device applications and fundamentally interesting features.[1–10] Under resonant optical excitation conditions, the photoexcited electrons and holes are not significantly exposed to scattering and intraband transitions. Therefore, polarization of the QD emission can be related to the excitation source polarization.[11] However, under off-resonant excitation conditions, the light source has a shorter wavelength than that of the QD emission (Fig. 1a). As a result, before excitons are formed, the information regarding the incident light polarization is lost mostly *via* scattering with longitudinal optical (LO) phonons.[11,12] Therefore, the orientations of the dipole moments of the excitons become random (Fig. 1b). Under these conditions, although spin-selective optical excitation favors certain carrier spin states, the intra-relaxation towards ground states prevents maintaining such information. A limited number of reports have addressed the control of QD emission polarization *via* off-resonant optical excitation. These include ref. 13 and 14 wherein coupled QDs were used to show the control of polarization anisotropy of their spontaneous emission by changing the polarization of the excitation source. The existing reports also include the application of charge-modulation to support the scattering process that is faster than those involved with LO phonons.[11,12]

Significant research efforts have been devoted to controlling the spontaneous emission of QDs using photonic bandgaps and plasmonic effects.[1–9,15] In these cases, spin information of the excitation source is not maintained, rather formation of excitons occurs under preferred dipole orientations or field properties. A prominent technique for this includes the application of highly polarization-dependent plasmonic effects.[16–20] These effects can support exciton–plasmon coupling that is capable of projecting the emission polarization of QDs along certain directions. Such a coupling is based on the interaction of the excitons in QDs with localized surface plasmons resonances (LSPRs) in metallic nanostructures. When LSPRs have similar energies to those of excitons (Fig. 1a), excitons can be generated with projected dipole preference. Metallic nanorods, in particular, support distinct transverse and longitudinal modes, and as such their coupling with QDs can lead to two perpendicular projections of their dipoles (Fig. 1c and d).[17,18]

Recently we demonstrated that a double-heterostructure consisting of a Si/Al oxide charge barrier and a Si/Au Schottky

[a] Department of Physics and Astronomy, University of Alabama in Huntsville, Huntsville, Alabama, 35899, USA. E-mail: seyed.sadeghi@uah.edu
[b] EOTECH, Ann Arbor, MI 48103, USA
[c] Department of Physics and Astronomy, University of Exeter, Exeter EX4 4QD, UK
[d] Department of Chemistry and Biochemistry, Stephenson Life Sciences Research Center, University of Oklahoma, Norman, OK 73019, USA

† Electronic supplementary information (ESI) available. See DOI: 10.1039/d1tc02532e

‡ Current address: II–VI Photonics Inc., Paignton, UK.

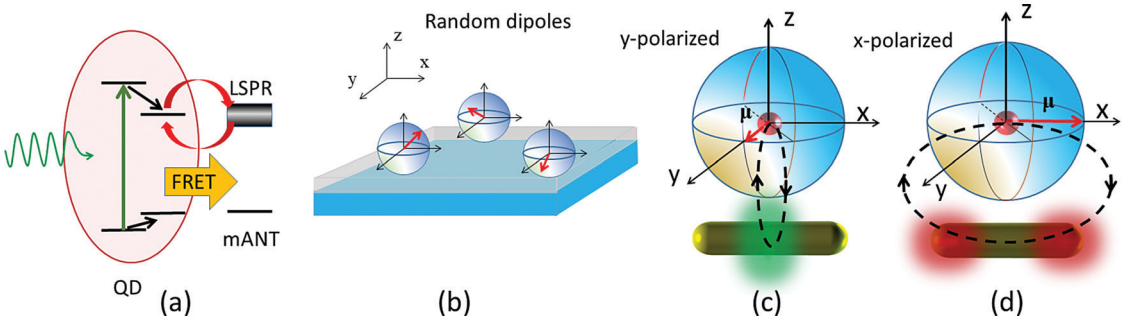

Fig. 1 (a) Schematic diagram of off-resonant excitation of QDs and the electron/hole relaxation towards the band gap. (b) Exciton dipoles with random directions after the relaxation processes in the absence of plasmonic structures. (c) and (d) Show the projection of the dipole moments of excitons by exciton–plasmon coupling for the cases when the exciton energies match the transverse and longitudinal modes of a mANT, respectively. The red curved arrows in (a) represent the exciton–plasmon coupling and FRET refers to the Förster resonance energy transfer.

junction allows one to utilize plasmonic effects to not only make QDs faster and highly polarized emitters, but also suppress the impact of defects.[17,21] Such structures, called metal-oxide plasmonic metasubstrates (MOPMs), consist of an array of metallic nanoantennas (mANTs), a Si embedding layer, and an ultrathin layer of Al oxide (Fig. 2a and b). The presence of the Au/Si junction allows the transfer of hot electrons, generated by non-radiative decay of plasmons, to the Si layer (Fig. 2c).[22–25] Such a process in the presence of a Si/Al oxide charge barrier, which supports high density negative surface charge distributions,[26,27] can lead to charging of the Si layer. This, in turn, leads to the formation of an electrostatic field,[28] which suppresses the migration of photo-excited electrons from the QDs to the defect sites. This process reduces the defect-induced non-radiative decay of QDs while the Purcell effect caused by the LSPRs continues to enhance the spontaneous emission decay rates of the QDs. Therefore, QDs become very efficient emitters.

In this paper we show that in a MOPM environment one can use the state of polarization of an off-resonance laser field to control not only the intensity but also the polarization of spontaneous emission of QDs. In other words, we demonstrate that a MOPM allows one to project certain polarization states into the spontaneous emission of QDs, maintaining the memory of their excited state polarization. Our results show that such a process occurs *via* the photonic lattice modes (PLMs) formed by the mANT arrays, enhancement of the exciton–plasmon coupling, and surface charges accumulated at the Si/Al oxide junction.

II Methodology

Three types of mANT arrays (samples 1–3) were fabricated using e-beam lithography. In sample 1, the average length (L) was ~310 nm and the average width (W) was ~110 nm. In addition its lattice constants along the x-axis (a_x) was 700 nm and along the y-axis (a_y) was 500 nm (Fig. 3a inset). In sample 2, $L \sim 885$ and $W \sim 220$ nm and $a_x = 1000$ and $a_y = 500$ nm (Fig. 3b inset). In sample 3, $L \sim 1370$ nm, $W \sim 260$ nm, $a_x = 1.4$ μm and $a_y = 500$ nm (Fig. 3c inset). After fabrication, these structures were covered with 15 nm Si and 1 nm of Al oxide using a sputtering machine (Fig. 2a). We previously demonstrated that such a thickness of Al oxide is optimized for the performance of MOPMs.[21] In fact the 1 nm deposition of Al forms nanoislands with heights of few nanometers. For thinner layers, the impact of Al oxide is much less. For thicknesses larger than 1 nm the impact of the accumulated defect sites overwhelms the effects of the surface charges, leading to strong suppression of the QD

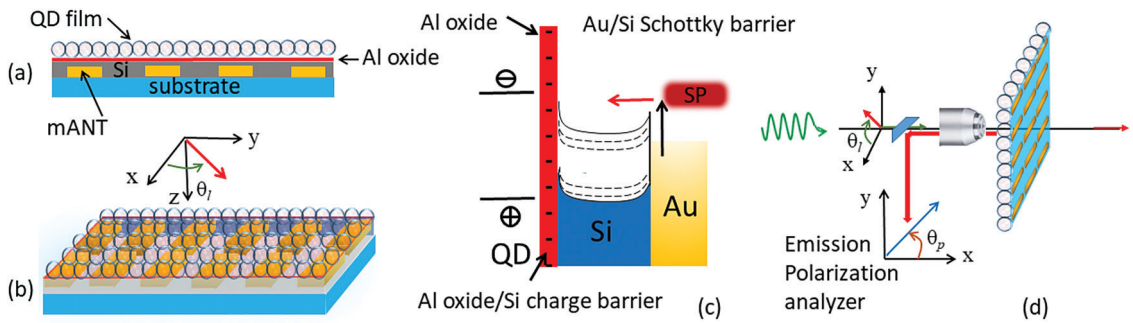

Fig. 2 (a) Cross-sectional view of a MOPM consisting of a glass substrate, an array of Au mANTs, a Si spacer, an ultrathin Al oxide layer, and a thin film of CdSe/ZnS QDs. (b) An oblique view of the structure depicting the arrival of a linearly polarized light. (c) Schematic illustration of the double-junction heterostructure consisting of a Si/Al oxide charge barrier and a Si/Au Schottky junction. (d) Schematic of the optical setup used for the detection of the emission of QDs on the MOPM. Here the incident laser beam polarization makes angle θ_l with respect to the long axis of mANTs (x-axis). A polarization analyzer with axis angle θ_p with respect to x-axis is used to analyze the state of polarization of the emission of QDs.

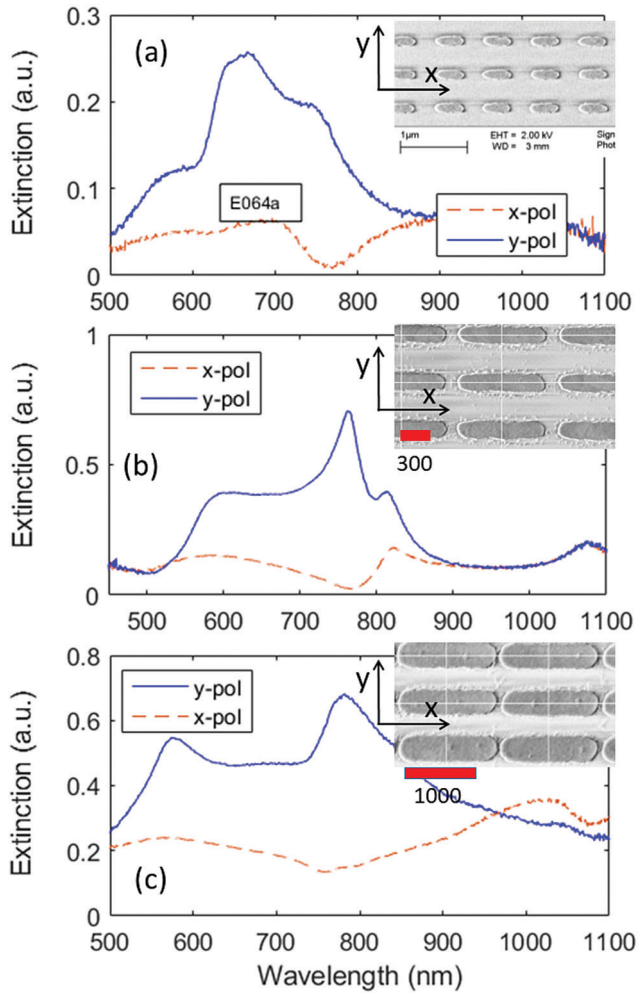

Fig. 3 (a)–(c) Extinction spectra of samples 1–3 for the x-pol (dashed line) and y-pol (solid line). The legends show the corresponding SEM images of the samples. The numbers under the red scale bars are in nm.

emission, before the mirror effect of the Al layer appears.[21] Similar samples without Al oxide were also fabricated as references. To obtain the extinction spectra of these arrays we used a transmission setup wherein the polarization of the incident white light source was controlled. As shown in Fig. 2b, we considered that the axis of polarization of this light made angle θ_l with respect to the long axes of the mANTs (x-axis).

After characterization of these samples, we spin coated QDs on the top of the Al oxide layers (Fig. 2a). The QDs were made up of CdSe cores and ZnS shells with octadecylamine ligands acquired from NN Lab, LLC. The central wavelength of their emission was around 635 nm, which was red-shifted from its absorption spectra by about 15 nm (Fig. S1, ESI†). These QDs were excited with a 514 nm laser and their emission was detected by using a thermoelectrically cooled spectrometer. To measure the decay of QDs, we used a time correlated single photon counting (TCSPC) system (Picoquant Pico-Timeharp 260) combined with a 30 ps 450 nm pulsed laser and a single photon avalanche detector (SPAD). The 514 nm laser field was linearly polarized, making angle θ_l with respect to the long axis of the mANTs or x-axis (Fig. 2b and d). We also used a microscope objective to collect the emission of QDs. After this light was reflected from a dichroic filter it was passed through a polarization analyzer before reaching the spectrometer (Fig. 2d). The axis of this analyzer with respect to the x-axis is denoted as θ_p.

The types of samples considered here provide diverse forms of plasmonic effects, from relatively localized ones (sample 1) to the case wherein it supported edge modes (sample 3). The extinction spectra of these samples with 15 Si are shown in Fig. 3a–c. These spectra are the average of four arrays. We noted that there was a drastic difference in the extinction spectra for the two perpendicular polarization cases. When the incident light was polarized along the x-axis (x-pol), *i.e.* $\theta_l = 0^\circ$, for the spectral range considered in Fig. 3, it did not excite any strong plasmonic effects. The small peaks seen in this case are associated with high order plasmonic standing modes of the samples.[29] When the incident light was polarized along the y-axis (y-pol), *i.e.*, $\theta_l = 90^\circ$, however, the responses of these samples were quite different. For sample 1, one can see a hump at 568 nm, a peak at 665 nm, and another hump at about 750 nm. For the case of sample 2, a similar situation to that in sample 1 happens. Here, however, the two humps, one at 600 nm and the other at about 810 nm, become more distinctively resolved. Additionally, a sharper peak is formed at about 766 nm. For the case of sample 3, the peaks at 573 and 782 nm represent two collective states with high and low refractive index sensitivities, respectively.[30] it is to be noted that we do not see any significant differences in the extinction spectra of the samples with and without the Al oxide layers.

III Excitation polarization memory

We are interested to show how, in the presence of a MOPM, one can use polarization of an off-resonant incident light to control the spontaneous emission of QDs. For this we analyze the emission intensity and polarization of the QDs deposited on the MOPMs outlined in the preceding section while the polarization of the excitation laser was rotated by angle θ_l (Fig. 2d). The intensity of the laser, however, was kept constant at 2 mW. For this, we measure the emission enhancement factor (E_{enh}), defined as the ratio of the emission of QDs in the presence of a MOPM to that of the QDs on a glass substrate with 15 nm of Si with the Al oxide layer. The results of samples 1–3 as a function of θ_p are shown in Fig. 4. In Fig. 4a–c, the circles and squares refer to the cases where the polarization axis of the excitation laser beam was along the x-axis ($\theta_l = 0^\circ$) or y-axis ($\theta_l = 90^\circ$), respectively. In the case of sample 1 (Fig. 4a), the results show that the overall value of E_{enh} is more for the case of $\theta_l = 90^\circ$. In this case, for $\theta_p = 0^\circ$ and 90°, these results suggest $E_{enh} \sim 4.3$ and 5.5, respectively.

The case of sample 2, however, offers a very different picture (Fig. 4b). The prominent features seen here include strong dependencies of both intensity (E_{enh}) and polarization of the

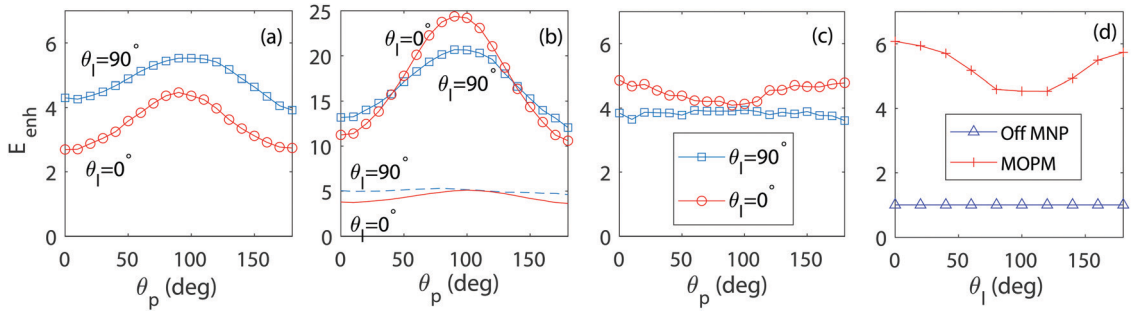

Fig. 4 The emission enhancement factors of QDs on samples 1–3 (a–c) as a function of θ_p. The circle and square lines refer to the cases when θ_l = 0 and 90°, respectively. The solid and dashed lines in (b) show the results for the enhancement factor when θ_l = 0 and 90° in the absence of Al oxide laser. (d) Emission of QDs on sample 3 when the analyzer in front of the spectrometer is removed and θ_l is varied between 0 and 180°.

QD emission on the polarization of the excitation laser. In fact, in this case when $\theta_l = 0°$ the value of E_{enh} at $\theta_p = 0°$ is about 11 and at $\theta_p = 90°$ it becomes about 25 (circles). On the other hand, when $\theta_l = 90°$, the values of E_{enh} for $\theta_p = 0°$ and 90° become about 13 and 20, respectively. These results indicate the efficient injection of the excitation laser polarization memory to the QD emission.

The situation becomes different for the case of sample 3. In this case E_{enh} reduces drastically. Quite interestingly, when $\theta_l = 0°$ this happens with a weak reversal of the dependency of E_{enh} on θ_p (circles). Additionally, when $\theta_l = 90°$, the value of E_{enh} becomes nearly independent of θ_p (squares). In other words, the emission of QDs becomes unpolarized. This presents the case wherein the incident laser polarization memory is weakly transferred to the emission of QDs.

IV Impact of photonic lattice modes

The results presented in the preceding section indicate how a MOPM can modify the spontaneous emission of QDs and transfer the polarization memory of excitation laser to their spontaneous emission. This process can be related to (i) photonic lattice modes (PLMs) generated by the arrays of mANTs, (ii) exciton–plasmon coupling, and (iii) the electron–electron scattering process. In this section we highlight the impact of PLMs, and in the following section we address (ii) and (iii).

To proceed further, it is to be noted that PLMs are formed *via* diffraction of light in the planes of periodic arrays of mANTs when the Rayleigh condition is satisfied.[31–33] Depending on the shapes of the mANTs, these modes can make the intensity of the spontaneous emission of QDs dependent on the state of the polarization of the excitation source, to some extent. This can be observed from Fig. 3b and c that, at a laser wavelength of 514 nm, the samples 2 and 3 do not support any significant polarization-dependent extinction. Despite this, the results presented in Fig. 4b and c show a clear dependency on the polarization of this laser. To show how this can be related to PLMs, we utilized finite difference time domain (FDTD) to study the optical and plasmonic field properties of the structures studied in this paper. For studying this, we used Device Suite of Lumerical 2020a. The simulation structures that represent samples 1–3 (Fig. 3a–c) are shown in Fig. 5a–c, respectively. The refractive index of the substrates was considered to be 1.45, as the same as that of glass. For the superstrate, however, we consider the effective refractive indices that allow the simulation results become similar to those shown in Fig. 3a–c (solid lines). This allows us to estimate the degree of accuracy of the simulation and the effective refractive indices associated with the 15 nm Si layers sputtered on the mANT arrays.

The simulation results for the structures shown in Fig. 5a–c are shown in Fig. 5a′–c′, respectively. Here the solid lines refer to the case when the incident light is polarized along the *y*-axis (*y*-pol) and dashed lines to the case of when it is polarized along the *x*-axis (*x*-pol), corresponding to $\theta_l = 90°$ and 0°, respectively. For the cases of samples 1 and 2 (Fig. 3a and b) good matches occur when the effective refractive index of the superstrate is considered to be 1.6 (Fig. 5a′ and b′). This seems to be reasonable considering the fact that although the refractive index of Si is high, the layer thicknesses were about 15 nm. For the case of sample 3 (Fig. 3c), however, the results offer a good match when the effective refractive index is about 1 (Fig. 5c′). When the refractive index increases to 1.3, the peak that was initially at about 550 nm is red-shifted significantly. This can be associated with the over-estimation of the mode profiles in the superstrate, giving rise to high refractive index sensitivity.[30]

Numerical calculations for the mode field enhancement factor, defined as the ratio of the field intensity in the presence of the mANT array to that in its absence, can reveal the key features of PLMs in the structures considered in Fig. 5. The results for the structure shown in Fig. 5a (sample 1) are presented in Fig. 6. When the incident light is polarized along the *x*-axis and its wavelength is 521 nm, Fig. 6a–c suggest weak photonic modes on the top of the mANTs. For the case of polarization along the *y*-axis the results offer slightly stronger fields (Fig. 6a′–c′). This may explain why for $\theta_l = 90°$ (*y*-pol) the values of E_{enh} in Fig. 4a (squares) seem to be larger than the case of $\theta_l = 0°$ (*x*-pol). Note that here the *x*–*y* plane passes through the middle of the mANTs, parallel to the plane of the array (Fig. 6a and a′). The *x*–*z* and *y*–*z* planes also pass through the middle of the mANTs but they are perpendicular to the array's plane and are parallel to the *x*- (Fig. 6b and b′) and *y*-axes (Fig. 6c and c′).

At 658 nm, *i.e.*, the typical emission wavelength of the QDs used in this paper, for both cases of *x*-pol and *y*-pol, *i.e.* $\theta_p = 0°$ and 90°, we can see clear formation of PLMs. In both cases these modes are

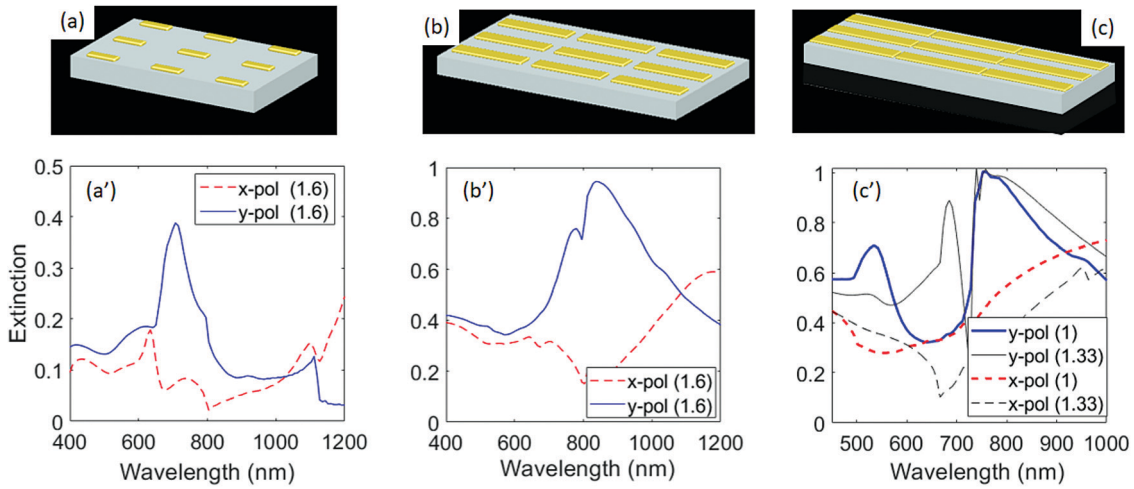

Fig. 5 (a and b) The simulation structures associated with samples 1–3. (a′–c′) The simulation results for the extinction spectra of these structures when the incident light is polarized along the *x*-axis (dashed lines) and *y*-axis (solid lines). The number in the parentheses in the legends refer to the effective refractive index of the superstrate.

coupled to the LSPRs of the mANTs. Comparison of Fig. 6d–f (*x*-pol) and Fig. 6d′–f′ (*y*-pol), however, suggests stronger field enhancement *via* LSPRs for the case of *y*-pol ($\theta_p = 90^\circ$). This explains that when excitons are formed, their dipole moments have more chance to be aligned along the *y*-axis. The increase of intensity for $\theta_p = 90^\circ$ seen in Fig. 4a for both $\theta_l = 0^\circ$ and 90° shows the overwhelming impact of this effect.

For the case of sample 2, Fig. 7a–d suggest that at 521 nm the PLMs are more pronounced for *x*-pol ($\theta_l = 0^\circ$) than *y*-pol ($\theta_l = 90^\circ$). Based on this one expects higher excitation enhancement of QDs when the incident light is polarized along the *x*-axis. This is particularly related to the presence of optical modes in the spacing between the mANTs (Fig. 7b). For *y*-pol, however, such modes are much weaker (Fig. 7d). Considering the fact that QDs located within such spacings can support stronger exciton-plamson coupling, one expects that they play a more dominant role in the formation of polarized spontaneous emission, as seen in Fig. 4b (circles).

The results of simulation at the emission wavelength of the QDs (650 nm) provide further evidence of the role played by PMLs and their coupling with LSPRs. For $\theta_p = 0^\circ$ (*x*-pol) we see the presence of photonic modes on the top and between the mANTs (Fig. 7a′ and b′). Considering the fact that QDs are more efficiently pumped when $\theta_l = 0^\circ$ (Fig. 7a and b), the coupling between PLM and LSPRs at 650 nm supports a rather high E_{enh}. This can explain the results seen in Fig. 4b when $\theta_p = 0^\circ$ and $\theta_l = 0^\circ$ and 90°. At this wavelength, for $\theta_p = 90^\circ$ (*y*-pol) the results suggest a stronger coupling between LSPRs and PLMs (Fig. 7c′ and d′). In the *x*–*z* plane (Fig. 7c′), this can happen around the edges of the mANTs. In the *y*–*z* plane (Fig. 7d′), the photonic modes on the top of the mANTs are well connected to the plasmon modes of the mANTs. Combination of these processes suggests that for $\theta_p = 90^\circ$ (*y*-pol), one would expect a higher degree of exciton–plasmon coupling. This process combined with the enhancement of exciton–plasmon coupling *via* MOPMs explains the significant increase of the emission enhancement of QDs when $\theta_p = 90^\circ$ (Fig. 4b). For $\theta_p = 0^\circ$, however, the emission enhancement is mostly related to the more prominent role of PLMs.

In regards to the structure shown in Fig. 5c, it is to be noted that when the mANTs have lateral dimensions much larger than their heights, *i.e.*, flat metallic nanoantennas (FmANTs), their modes can be decomposed into two main categories, *i.e.*, edge and cavity modes.[34–36] The edge plasmon modes are concentrated at the edges of the FmANTs and can have various multipolar characters. The cavity or breathing modes, on the other hand, are concentrated at the center of the FmANTs.[34] Previous studies have shown that QDs can get coupled to the edge modes and even transfer their energies to FmANTs.[37] Fig. S2 in the ESI† shows the mode profiles of the structure shown in Fig. 5c at 569, 660, and 775 nm for *x*-pol ((a)–(c)) and *y*-pol ((a′)–(c′)) in the *y*–*z* plane. The results show clear differences between the *x*-pol and *y*-pol cases. At 569 nm, for *x*-pol, we can see a clear presence of fields between the mANTs (Fig. S2a–c, ESI†). This particularly is more prominent at 660 and 775 nm. For the case of *y*-pol, on the other hand, there is nearly no field in the spacing between the FmANTs (Fig. S2a′–c′, ESI†).

The results shown in Fig. S2 of the ESI† suggest that in the case of *x*-pol, *i.e.*, $\theta_l = 0^\circ$, there is no significant coupling between the plasmonic field and photonic modes. This highlights the fact that for such a polarization, one mostly deals with PLMs. In the case of *y*-pol ($\theta_l = 90^\circ$), however, there is some limited amount of such a coupling, particularly at 660 nm. To observe the impact of such PLMs on the optical excitation of sample 3 further, we removed the polarization analyzer of the QDs, allowing their emission to reach the spectrometer directly. Under this condition we rotated the polarization of the incident laser, changing θ_l from 0° to 180°, while measuring the emission of the QDs. The results in Fig. 4d show that for QDs on a glass/Si/Al oxide substrate, the value of θ_l has no impact (triangles). This emphasizes the fact that the excitation of single QDs with nearly spherical shapes is independent of polarization

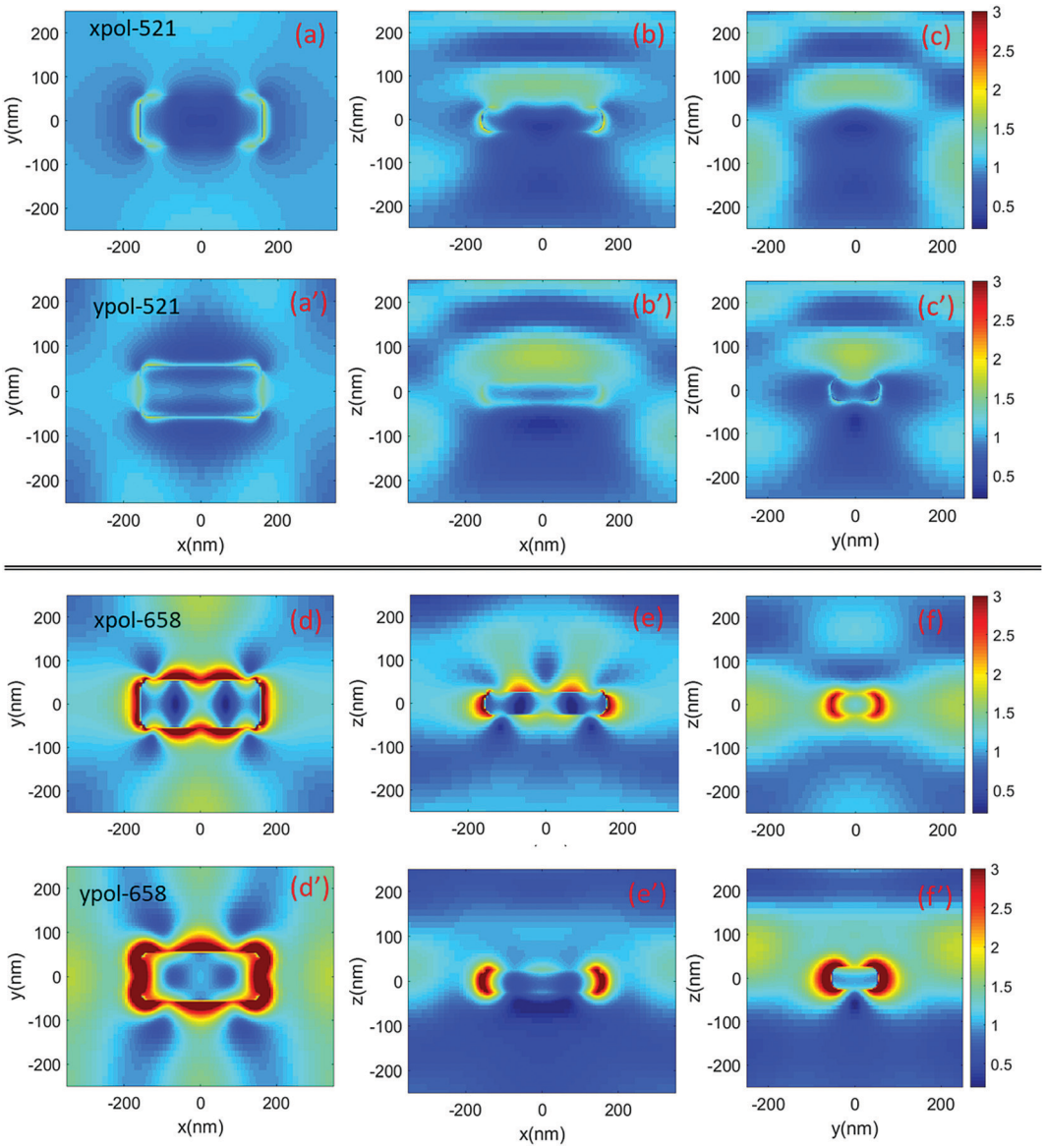

Fig. 6 Mode field enhancement profiles in the x–y, x–z, and y–z planes for the structure shown in Fig. 5a when the incident light wavelength is 521 nm and is polarized along the x-axis ((a)–(c)) and y-axis ((a′)–(c′)). (d)–(f) and (d′)–(f′) are similar to (a)–(f) and (a′)–(c′) but when the wavelength of incident light is 658 nm, respectively.

of the excitation light source. For the case of QDs on MOPMs, however, the maximum of E_{enh} occurs at $\theta_l = 0^\circ$ and 180° (crosses). When the incident laser is polarized along the y-axis, *i.e.*, $\theta_l = 90^\circ$, the emission enhancement decreases by about 30%. This highlights the fact that in the presence of arrays of flat mANTs, the excitation field experienced by the QDs becomes quite polarization-dependent, as suggested by Fig. S2 (ESI†).

V Hot electron-induced electrostatic field and charging effects

Previously we have shown that excitons in the presence of a MOMP with mANT arrays as in sample 2 can live longer than those in QDs placed on a glass/Si/Al oxide substrate.[17,21] As shown in Fig. 8a, a similar process can also happen to a MOPM having mANT arrays as in sample 3. Here line 1 refers to the decay of QDs on the MOPM and line 2 to that of QDs on a glass/Si Al oxide substrate. The wavelength dependency of decay of such QDs is shown in the ESI† (Fig. S3). The lifetime enhancement seen in Fig. 8a occurs despite the fact that both Förster resonance energy transfer (FRET) from QDs to mANTs (Fig. 1a) and the Purcell effect tend to reduce the lifetime of the QDs. As discussed in ref. 21 and 17, such a process can be associated with the hot-electrons generated by the non-radiative decay of plasmons. In the presence of the Schottky barrier, these electrons can be captured by the Si layer, leading to charge accumulation (Fig. 2c and 8b). This process generates an

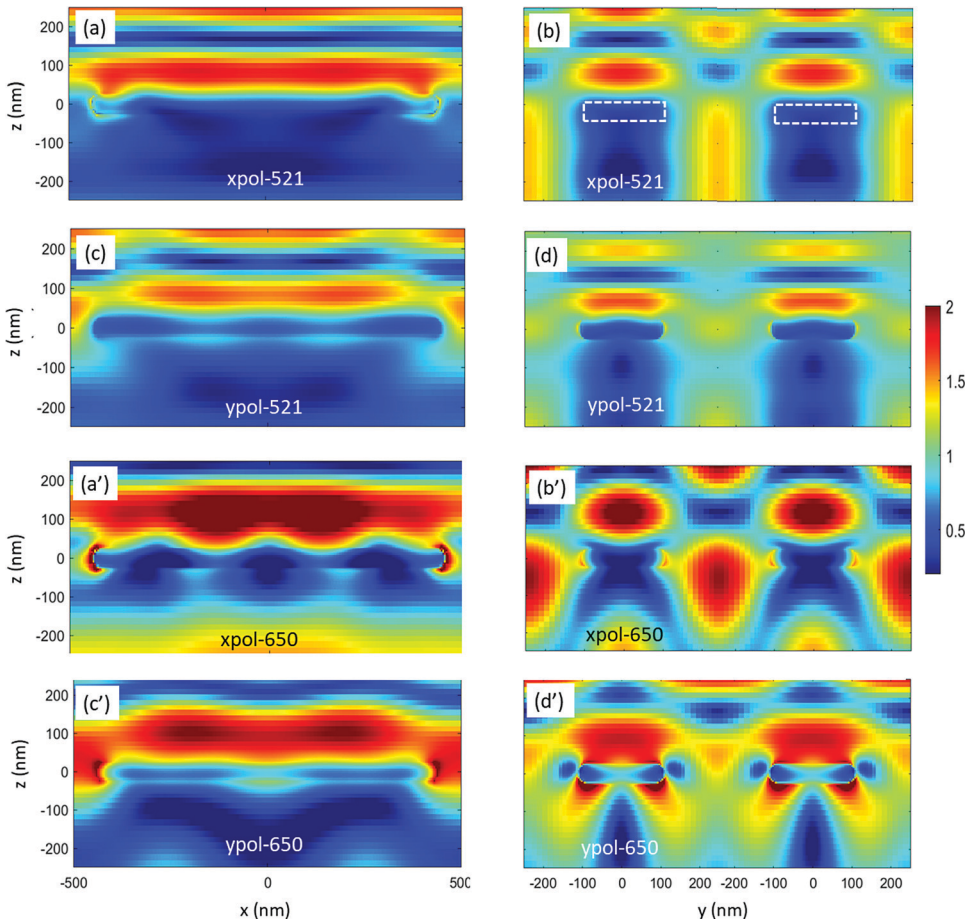

Fig. 7 Mode field enhancement profiles for the structure shown in Fig. 6b, corresponding to sample 2, at 521 nm when the incident light is polarized along the *x*-axis (a) and (b) and *y*-axis ((c) and (d)). (a′), (b′), (c′) and (d′) are similar to (a), (b), (c) and (d), respectively, but at 650 nm. (a), (c), (a′) and (c′) show the mode profiles in unit cells in the *x*–*y* plane while (b), (d), (b′) and (d′) represent two unit cells.

electrostatic field that can suppress the migration of electrons from QDs to the defect sites.[28] Under these conditions, the excitons are quarantined against their defect environment and the rates of migration of the photo-excited electrons to the defects in the substrate (k_{f1}) and QD surface traps (k_{f2}) are suppressed (Fig. 8b).

The relative variations of the defect sites and non-radiative decay rates of QDs on MOPMs *versus* those on the glass/Si/Al oxide substrate can be clarified further using a biexponential fitting, $I(t) = C_f e^{-t/\tau_f} + C_s e^{-t/\tau_s}$. Here C_f and τ_f refer to the amplitude and decay time of the non-radiative decay processes, respectively, and C_s and τ_s to those of radiative decay.[38,39] After applying this fit to the data shown in Fig. 8a we found that in the absence of a MOPM, the ratio C_f/C_s is 1.95. In the presence of a MOPM, this ratio reduces to 1.82, indicating a decrease of the defect sites. On the other hand, the values of τ_f in the absence of a MOPM is found to be about 2.28 ns, while in the presence of a MOPM it increases to 2.94 ns. The combination of these makes the impact of the non-radiative decay associated with defect sites less prominent.

To model the formation of the electrostatic field by hot electrons, it is to be noted that the decay of plasmons leads to the generation of electron/hole pairs. Capturing the electrons using the Schottky barrier can be related to the incident photon-to-electron conversion efficiency (IPCE) studied in photovoltaic devices.[40] Since such a process leaves holes in the metal side, its overall impact is the formation of positive and negative Coulomb potentials in the structure. The range of the impact of the electrons trapped in the Si layer can be analyzed considering the potential associated with an electron in this layer, which is represented by $V_e(r) = k\frac{-e}{|\mathbf{r}-\mathbf{r}'|}$. The hole potential is given by $V_h(r) = k\frac{e}{|\mathbf{r}|}$. Here $\mathbf{r}$ represents the distance of a point of observation above the Si layer from the hole location, and $\mathbf{r}'$ is the hot electron and hole distance. Considering these, the overall potential on the top of the Si layer is $V = V_- + V_+$.

To continue our analysis, we considered the thickness of the Si layer to be 15 nm, as in the experimental part, and the hole was located at 2 nm below the Si/Au interface, inside the Au layer. Fig. 8c and d show two cases wherein the electron counterpart in the Si layer is located at 10 and 15 nm from the Au/Si interface, respectively. The circles in these figures

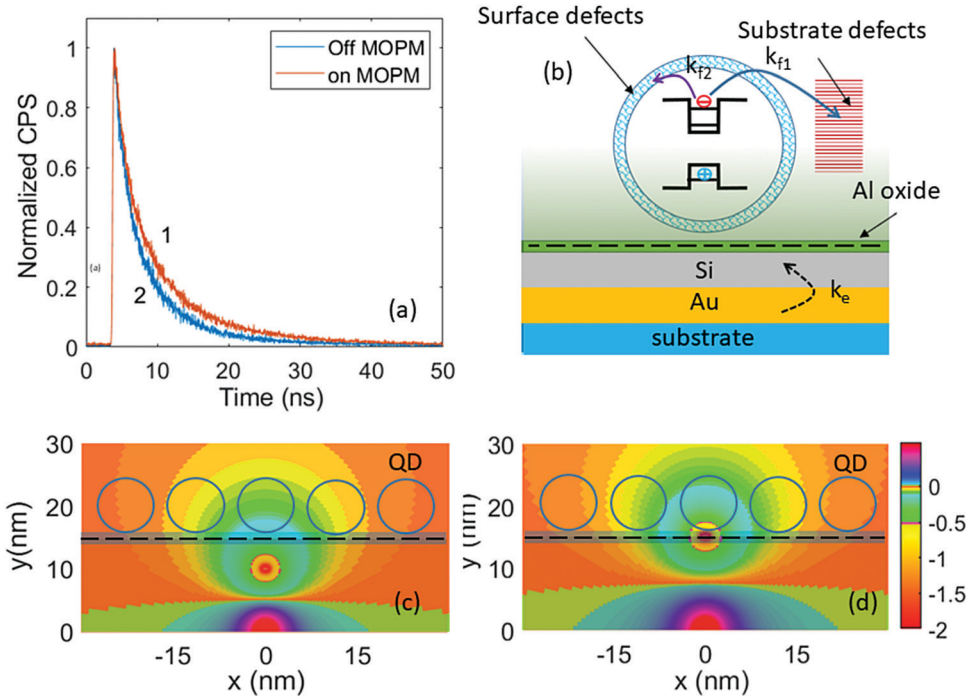

Fig. 8 (a) Decay of QDs on sample 3 (line 1) and on a glass/Si/Al oxide substrate (line 2). (b) Schematic of a QD in the presence of its defect environment (DE) and a MOPM. Simulation of electrostatic field distributions when an electron is trapped at 10 and 15 nm from the surface of the mANT. The hole is assumed to be located at 2 nm below the Au surface. The circles in (c) and (d) refer to the scale of QDs.

show the spatial extent of the QDs. The results suggest that, depending on the position of the trapped electron, the number of QDs influenced by the electrostatic field is different. Considering that the thickness of the Al oxide layer is rather small and it is charged, one expects that the case shown in Fig. 8d occurs more. In fact, the surface charges of the Si/Al oxide layer (Fig. 8b), by themselves can, to some extent, suppress the migration rates, k_{f1} and k_{f2}.[41] In the case of MOPMs, the hot electrons transferred to the Si layer and trapped at the Si/Al oxide interface can further enhance the suppression of the migration of photo-excited electrons from QDs (k_{f1} and k_{f2}). This leads to the suppression of the Auger recombination, enhancing their emission. The details of the model that shows how such electrostatic potentials can reduce the rate of transfer of photo-excited electrons from QDs to trap states are presented in ref. 28.

Considering all these factors mentioned above, the polarization memory seen in Fig. 4b may be related to the relaxation of electron/hole pairs in the QDs in the presence of the plasmonic double junction structure (MOPM). Recent reports have explored the impact of surplus carriers generated by modulation-doping on the intradot relaxation mechanisms.[11,12,42] They have shown that the impact of phonon-mediated cascade relaxation, which is dominant in undoped structures, can be suppressed by scattering of the built-in carriers. This can lead to the preservation of spin polarization during energy relaxation.[43] Previous studies have also shown that the surface charges in the Si/Al oxide layer reside at a few nanometers from the surface of the Al oxide layer,[44] imitating the case shown in Fig. 8d. Therefore, considering the cross-section of electron–electron scattering in QDs to be around 40 nm^2,[45] one expects that such electron–electron scattering can reduce the spin relaxation. This seems to be also consistent with the previous reports that showed that a two-dimensional electron gas can extend the spin lifetimes.[46,47]

A key feature of the results seen in Fig. 4 is the enhancement of exciton–plasmon coupling *via* MOPMs. This can be seen vividly in the case of sample 2. To verify this, in Fig. 4b, we show the results of the reference sample which had similar structures to that of sample 2, but without the Al oxide layer (solid and dashed lines). One can see here that the lack of this layer leads to a much less amount of E_{enh} and far less polarized emission. This suggests that the presence of the charged Si layer and the Si/Al oxide significantly enhances exciton–plasmon coupling, allowing far more efficient projection of exciton dipoles once they are formed at the band edge of the QDs (Fig. 1c).[17] This feature explains the variations of E_{enh} with θ_p for a given value of θ_i.

VI Conclusions

We investigated the application of metal-oxide plasmonic substrates for the preservation of spin polarization of QDs when they were excited off-resonantly. The results showed that the impact of Si/Au and Si/Al oxide double junctions in such structures can include the partial recovery of the spin polarization. Our results revealed the role played by the photonic lattice modes in making off-resonant optical excitation of QDs dependent on the excitation light polarization. We discussed the

impact of electron concentration in the Si layer and at the Si/Al oxide interface on the transfer of the optical excitation memory to the spontaneous emission of QDs.

Conflicts of interest

There are no conflicts to declare.

Acknowledgements

This work is supported by the US National Science Foundation under grants ECCS-1917544 and ECCS-1917037.

References

1 C. DiLoreto and C. Rangan, *Phys. Rev. A*, 2017, **95**, 043834.
2 D. Englund, D. Fattal, E. Waks, G. Solomon, B. Zhang, T. Nakaoka, Y. Arakawa, Y. Yamamoto and J. Vuć, *Phys. Rev. Lett.*, 2005, **95**, 013904.
3 M. G. Dutt, J. Cheng, B. Li, X. Xu, X. Li, P. Berman, D. Steel, A. Bracker, D. Gammon and S. E. Economou, *et al.*, *Phys. Rev. Lett.*, 2005, **94**, 227403.
4 D. Unitt, A. Bennett, P. Atkinson, D. Ritchie and A. Shields, *Phys. Rev. B: Condens. Matter Mater. Phys.*, 2005, **72**, 033318.
5 R. Oulton, B. Jones, S. Lam, A. Chalcraft, D. Szymanski, D. O'Brien, T. Krauss, D. Sanvitto, A. Fox and D. Whittaker, *et al.*, *Opt. Express*, 2007, **15**, 17221–17230.
6 M. Ren, M. Chen, W. Wu, L. Zhang, J. Liu, B. Pi, X. Zhang, Q. Li, S. Fan and J. Xu, *Nano Lett.*, 2015, **15**, 2951–2957.
7 E. Gallardo, L. Martnez, A. Nowak, H. Van der Meulen, J. Calleja, C. Tejedor, I. Prieto, D. Granados, A. G. Taboada and J. Garca, *et al.*, *Opt. Express*, 2010, **18**, 13301–13308.
8 W.-H. Chang, W.-Y. Chen, H.-S. Chang, T.-P. Hsieh, J.-I. Chyi and T.-M. Hsu, *Phys. Rev. Lett.*, 2006, **96**, 117401.
9 C. Lai, P. Maletinsky, A. Badolato and A. Imamoglu, *Phys. Rev. Lett.*, 2006, **96**, 167403.
10 D. P. DiVincenzo, *J. Appl. Phys.*, 1999, **85**, 4785–4787.
11 S. Marcinkevičius, J. Siegert and Q. X. Zhao, *J. Appl. Phys.*, 2006, **100**, 054310.
12 J. Siegert, S. Marcinkevičius and Q. X. Zhao, *Phys. Rev. B: Condens. Matter Mater. Phys.*, 2005, **72**, 085316.
13 H. Kim, I. Kim, K. Kyhm, R. A. Taylor, J. S. Kim, J. D. Song, K. C. Je and L. S. Dang, *Nano Lett.*, 2016, **16**, 7755–7760.
14 H. Kim, K. Kyhm, R. A. Taylor, J. S. Kim, J. D. Song and S. Park, *Light: Sci. Appl.*, 2020, **9**, 1–10.
15 P. Mrowiński, M. Emmerling, C. Schneider, J. P. Reithmaier, J. Misiewicz, S. Höfling and G. Sęk, *Phys. Rev. B: Condens. Matter Mater. Phys.*, 2018, **97**(16), 165427.
16 H. Mertens, J. S. Biteen, H. A. Atwater and A. Polman, *Nano Lett.*, 2006, **6**, 2622–2625.
17 S. M. Sadeghi, W. J. Wing, R. R. Gutha, R. W. Goul and J. Z. Wu, *Phys. Rev. Appl.*, 2019, **11**, 024045.
18 Y.-C. Yao, Z.-P. Yang, J.-M. Hwang, H.-C. Su, J.-Y. Haung, T.-N. Lin, J.-L. Shen, M.-H. Lee, M.-T. Tsai and Y.-J. Lee, *Adv. Opt. Mater.*, 2017, **5**, 1600746.
19 Y. C. Jun, R. Pala and M. L. Brongersma, *J. Phys. Chem. C*, 2010, **114**, 7269–7273.
20 Y. Choi, T. Kang and L. P. Lee, *Nano Lett.*, 2008, **9**, 85–90.
21 S. M. Sadeghi, W. J. Wing, R. R. Gutha, J. S. Wilt and J. Z. Wu, *Nanoscale*, 2018, **10**, 4825–4832.
22 M. L. Brongersma, N. J. Halas and P. Nordlander, *Nat. Nanotechnol.*, 2015, **10**, 25.
23 R. Sundararaman, P. Narang, A. S. Jermyn, W. A. Goddard III and H. A. Atwater, *Nat. Commun.*, 2014, **5**, 5788.
24 W. Li and J. G. Valentine, *Nanophotonics*, 2017, **6**, 177.
25 M. W. Knight, H. Sobhani, P. Nordlander and N. J. Halas, *Science*, 2011, **332**, 702–704.
26 B. Hoex, J. Gielis, M. Van de Sanden and W. Kessels, *J. Appl. Phys.*, 2008, **104**, 113703.
27 B. Hoex, S. B. S. Heil, E. Langereis, M. C. M. van de Sanden and W. M. M. Kessels, *Appl. Phys. Lett.*, 2006, **89**, 042112.
28 S. M. Sadeghi, R. R. Gutha and C. Mao, *Adv. Mater. Interfaces*, 2020, **7**, 1901998.
29 E. K. Payne, K. L. Shuford, S. Park, G. C. Schatz and C. A. Mirkin, *J. Phys. Chem. B*, 2006, **110**, 2150–2154.
30 S. M. Sadeghi, W. J. Wing, R. R. Gutha, C. Sharp and A. Hatef, *J. Appl. Phys.*, 2017, **122**, 063102.
31 S. M. Sadeghi, R. R. Gutha, C. Sharp and A. Hatef, *Opt. Mater.*, 2018, **85**, 356–362.
32 Q.-Y. Lin, Z. Li, K. A. Brown, M. N. O'Brien, M. B. Ross, Y. Zhou, S. Butun, P.-C. Chen, G. C. Schatz, V. P. Dravid, K. Aydin and C. A. Mirkin, *Nano Lett.*, 2015, **15**, 4699–4703.
33 H. Saito, D. Yoshimoto, H. Lourenco-Martins, N. Yamamoto and T. Sannomiya, *ACS Photonics*, 2019, **6**, 2618–2625.
34 E. P. Bellido, A. Manjavacas, Y. Zhang, Y. Cao, P. Nordlander and G. A. Botton, *ACS Photonics*, 2016, **3**, 428–433.
35 A. Campos, A. Arbouet, J. Martin, D. Gerard, J. Proust, J. Plain and M. Kociak, *ACS Photonics*, 2017, **4**, 1257–1263.
36 E. P. Bellido, Y. Zhang, A. Manjavacas, P. Nordlander and G. A. Botton, *ACS Photonics*, 2017, **4**, 1558–1565.
37 S. M. Sadeghi, R. R. Gutha, W. J. Wing, C. Sharp, L. Capps and C. Mao, *J. Phys. D: Appl. Phys.*, 2017, **50**, 145401.
38 V. Klimov, D. McBranch, C. Leatherdale and M. Bawendi, *Phys. Rev. B: Condens. Matter Mater. Phys.*, 1999, **60**, 13740.
39 S. Brovelli, R. D. Schaller, S. Crooker, F. Garca-Santamara, Y. Chen, R. Viswanatha, J. A. Hollingsworth, H. Htoon and V. I. Klimov, *Nat. Commun.*, 2011, **2**, 1–8.
40 C. Clavero, *Nat. Photonics*, 2014, **8**, 95.
41 K. Patty, S. M. Sadeghi, A. Nejat and C.-B. Mao, *Nanotechnology*, 2014, **25**, 155701.
42 J. Fabian and S. D. Sarma, *J. Vac. Sci. Technol., B: Microelectron. Nanometer Struct.–Process., Meas., Phenom.*, 1999, **17**, 1708–1715.
43 S. Sato, S. Hiura, J. Takayama and A. Murayama, *Appl. Phys. Lett.*, 2020, **116**, 182401.
44 D. K. Simon, P. M. Jordan, T. Mikolajick and I. Dirnstorfer, *ACS Appl. Mater. Interfaces*, 2015, **7**, 28215–28222.
45 N. Tkach and J. Seti, *Semiconductors*, 2009, **43**, 340–346.
46 J. Kikkawa and D. Awschalom, *Phys. Rev. Lett.*, 1998, **80**, 4313.
47 J. Kikkawa, I. Smorchkova, N. Samarth and D. Awschalom, *Science*, 1997, **277**, 1284–1287.